Preparation, structure and luminescent performance of Na_2SiF_6:Re^{3+} (Re^{3+} = Eu^{3+}, Tb^{3+}, Ce^{3+}) powders

Jin-Yu Zhao[1] · Xi-Gui Wang[1]

Abstract

A series of Na_2SiF_6:xRe^{3+} (Re^{3+} = Eu^{3+}, Tb^{3+}, Ce^{3+}) phosphors were prepared by co-precipitation method. The structure and luminescence performance of the materials were characterized by XRD, TG–DSC, TEM, HRTEM, EDS, FT-IR, fluorescence spectra and the calculated CIE coordinates. The results show that under the excitation of specific UV light, Na_2SiF_6:xEu^{3+}, Na_2SiF_6:yTb^{3+} and Na_2SiF_6:zCe^{3+} single-doping materials exhibit the characteristic emission of Eu^{3+} ($^5D_0 \rightarrow {}^7F_2$, red), Tb^{3+} ($^5D_4 \rightarrow {}^7F_5$, green) and Ce^{3+} ($5d \rightarrow 4f$, blue), respectively. In the Na_2SiF_6:xEu^{3+}–yTb^{3+}–zCe^{3+} three-doping system, Na_2SiF_6:$0.03Eu^{3+}$–$0.07Tb^{3+}$–$0.07Ce^{3+}$ material is representative. With the increase of exciting wavelength of UV light, the emission color of the material realizes tunable from white light to cool white light, warm white light and red orange light. And the luminescence of the material is closest to the ideal white light under excitation of UV light at 290 nm. So this phosphor can be promised as a single-component tunable white phosphor for application in white LEDs.

1 Introduction

As a new generation of solid-state lighting source, white LED has been widely used in lighting, indicating, decoration and other fields, due to its energy saving, environmental protection, high efficiency and other performance [1, 2]. There are many kinds of processes for synthesizing white light [3, 4], e.g., in a combination of single red, green and blue LED chips, due to the different external voltages driving different chips, the electronic devices are complicated and difficult to simplify. This limits its development. Similarly, in a combination of a yellow phosphor and a blue LED chip, due to the lack of red light in the spectrum, the color temperature is high, the color is cold, and the color rendering index is poor; its development is also limited. Moreover, in a combination of three-color phosphors and a UV-LED chip, the white light of various color temperatures and color renderings can be obtained by adjusting the ratio of the three phosphors, thereby meeting the requirements of different lighting environments; however, this method has problems in color reabsorption and adjustment of the ratio. Therefore, developing a single-component white phosphor has become a hot topic in the research field of the current luminescent materials.

The phosphor consists of a host compound (i.e., a matrix moiety) and an active dopant (i.e., a luminescent center ion), sometimes doped with a sensitizer (i.e., another impurity ion to transfer energy) [5]. Rare earth ions have an unfilled $4f5d$ electronic configuration which is shielded from the outside. This leads to the rich electronic transitions. Among them, Eu^{3+}, Tb^{3+}, and Ce^{3+} are often selected as luminescent centers as rare earth ions capable of emitting red, green, and blue primary colors, respectively [6, 7]. Ren et al. [8] synthesized the Ce–Tb–Eu co-doped calcium borosilicate white light material, and studied the effect of Eu_2O_3 concentration on the luminescence performance of the material. Zhu et al. [9] studied the Ce–Tb–Eu co-doped silicate and phosphate white light materials. But the blue component of the photoluminescence spectrum was relatively strong, and the green and red components were relatively weak, resulting the color coordinates relatively poor. Ghosh et al. [10] synthesized the Ce–Tb–Eu co-doped zinc fluorosilicate white light material, which could obtain warm white light at 378 nm excitation. Subsequently, more researchers have studied fluorosilicate phosphors, and the results show that the doping of fluoride

✉ Xi-Gui Wang
 wangxg@imnu.edu.cn

[1] College of Chemistry and Environment Science, Inner Mongolia Normal University, Hohhot 010022, China

ion can improve the luminescence performance of the silicate phosphors. That is, the fluorosilicate phosphor is a new kind of promising luminescent materials.

Therefore, in this paper, the Na_2SiF_6 was used as the main matrix, and Eu^{3+}, Tb^{3+}, and Ce^{3+} were selected as luminescent centers. A series of rare earth ions single-doped red, green and blue monochromatic phosphors (i.e., $Na_2SiF_6:xEu^{3+}$, $Na_2SiF_6:yTb^{3+}$ and $Na_2SiF_6:zCe^{3+}$) were synthesized by co-precipitation method, respectively. Then, by further analyzing the energy transfer process between the three ions to adjust their metering ratio, a white phosphor which could be excited by 290 nm was synthesized. Moreover, according to the difference of energy transfer efficiency between the three ions under the excitation of UV light of different excitation wavelengths, a white phosphor which could change the emitting color of the phosphor by changing the excitation wavelength of UV light was obtained. That is $Na_2SiF_6:0.03Eu^{3+}–0.07Tb^{3+}–0.07Ce^{3+}$ phosphor.

2 Experimental part

2.1 Reagents and instruments

H_2SiF_6 and $Na_2SO_4·10H_2O$ (all AR) were, respectively, formulated into 0.20 mol/L H_2SiF_6 and Na_2SO_4 solutions; Eu_2O_3, Tb_4O_7 ($\geq$ 99.999%), HCl (12 mol/L) and $Ce(NO_3)_3$ were, respectively, formulated into 0.10 mol/L $EuCl_3$, $TbCl_3$ and $Ce(NO_3)_3$ solutions; absolute ethanol (AR, $\geq$ 99.7%).

XRD (Japan Ultima VI type, ray source Cu Kα, radiation wavelength λ = 0.15406 nm, tube voltage 40 kV, tube current 40 mA, scanning range 2θ = 10°–80°, scanning speed 10°/min), TG–DSC (France Setaram Labsys Evo type, air flow 30 mL/min, heating rate 10 °C/min), TEM equipped with EDS (Japan JEOL-2010 type, magnification × 50–1,500,000, acceleration voltage 200 kv), FT-IR (USA Nicolet, 6700 type, scanning times 32, resolution 4 cm^{-1}, KBr tablet method), fluorescence spectrometer (Japan Model FL-4500 type, Xe lamp source, PMT voltage 400 V, scanning speed 1200 nm/min, slit width 5.0 nm; UK Edinburgh, FLS-920 type, Xe lamp source, grating Ex/Em = 1/2, bandwidth Ex/Em = 10).

2.2 Preparation of materials

A series of $Na_2SiF_6:xRe^{3+}$ (Re^{3+} = Eu^{3+}, Tb^{3+}, Ce^{3+}) materials were synthesized by co-precipitation method. We prepared the matrix Na_2SiF_6 according to the reaction principle of $Na_2SO_4 + H_2SiF_6 = Na_2SiF_6\downarrow + H_2SO_4$. First, the known quantities Na_2SO_4 and H_2SiF_6 were reacted in a thermostat water bath beaker at 60–80 °C for 1 h, and then certain amounts of $EuCl_3$, $TbCl_3$ and $Ce(NO_3)_3$ were added for 1 h. After that, the reaction solution was cooled to room

temperature, filtered at normal pressure, washed three times with absolute ethanol, dried at room temperature, and thoroughly ground in an agate mortar to obtain a white powder solid. The solid was then annealed at 200, 300, 400, 500, 600, 700 and 800 °C for 2 h to obtain materials at different annealing temperatures, and the phase analysis was carried out to determine the optimum annealing temperature of the material. Finally, the material at the optimum annealing temperature was further selected for various optical and spectral characterizations.

3 Results and discussion

3.1 Structural analysis of $Na_2SiF_6:xRe^{3+}$ (Re^{3+} = Eu^{3+}, Tb^{3+}, Ce^{3+}) materials

Figure 1a shows XRD patterns of the Na_2SiF_6 materials at different annealing temperatures. It can be seen that all diffraction peaks of the Na_2SiF_6 materials after annealing at 200 °C, 300 °C and 400 °C can be indexed to the Na_2SiF_6 [11, 12] (JCPDS no. 33–1280), corresponding to the hexagonal phase (the space group is P321, the lattice constants are $a = b = 8.866$ Å, $c = 5.043$ Å). In the structure, each Si^{4+} is connected with six F^-, forming a regular SiF_6^{2-} octahedron, and two Na^+ are, respectively, located on both sides of the octahedral structure, and the crystal structure is highly symmetrical. However, as the annealing temperature increases again, the crystal structure of the Na_2SiF_6 material gradually decomposes. When annealing at 500 °C, a part of diffraction peaks of the material can correspond to the NaF (JCPDS no. 36–1455). That is, the matrix Na_2SiF_6 begins to decompose at this temperature ($Na_2SiF_6 \xrightarrow{\Delta} 2NaF + SiF_4\uparrow$) [13]. This phenomenon can be confirmed in the TG–DSC test of the Na_2SiF_6 material. Therefore, the optimum annealing temperature of the Na_2SiF_6 material is 400 °C, at this time, the material has good crystallinity and few miscellaneous peaks.

Figure 1b shows TG–DSC patterns of the Na_2SiF_6 material. In the temperature range of 35–150 °C, the obvious weight loss process of the TG curve and the distinct endotherm peak of the DSC curve can be seen in the picture, which are related to the loss of crystal water [14]. In the temperature range of 150–400 °C, there are no significant change in the TG and DSC curves, corresponding to the hexagonal Na_2SiF_6 crystal (JCPDS no. 33–1280). That is, the system is basically in a stable state. In the temperature range of 500–600 °C, the DSC curve shows an obvious endothermic peak, and the corresponding TG curve also shows an obvious phenomenon of weight loss, which are related to the decomposition of the Na_2SiF_6 crystal. Combined with Fig. 1a, we know that Na_2SiF_6 decomposes to form NaF (JCPDS no. 36–1455) [13], producing SiF_4 gas. When the
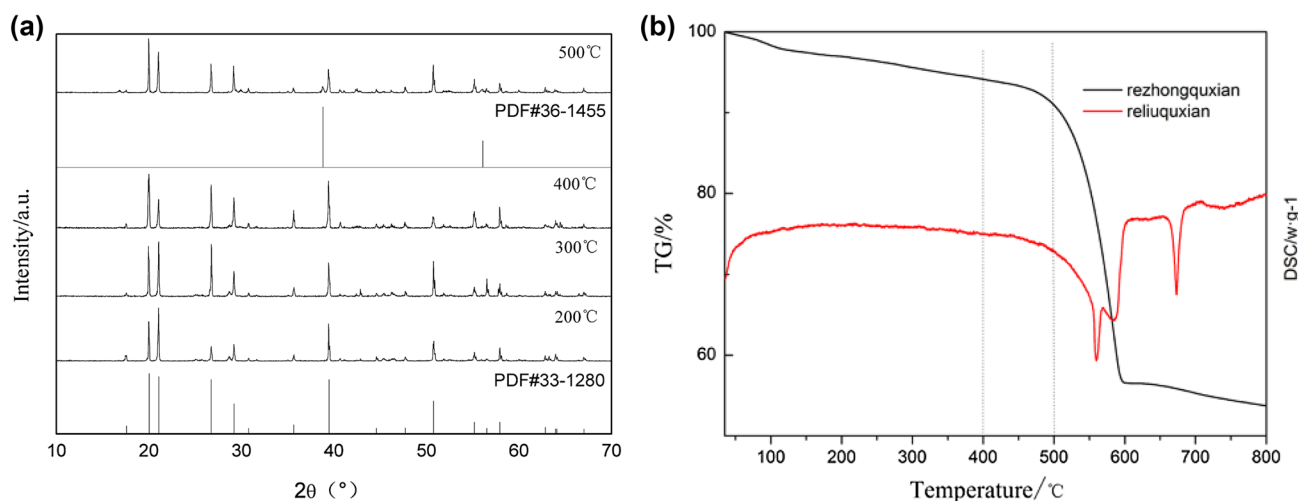
Fig. 1 XRD patterns of the Na$_2$SiF$_6$ materials annealed at different temperatures (200 °C, 300 °C, 400 °C, 500 °C) for 2 h (**a**) and TG–DSC patterns of the Na$_2$SiF$_6$ material (**b**)
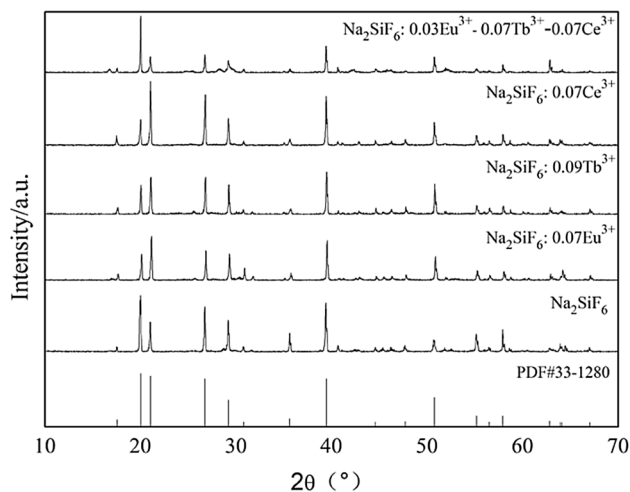

Fig. 2 Representative XRD patterns of the Na$_2$SiF$_6$:xRe^{3+} materials (i.e., Na$_2$SiF$_6$, Na$_2$SiF$_6$:0.07Eu^{3+}, Na$_2$SiF$_6$:0.09Tb^{3+}, Na$_2$SiF$_6$:0.07Ce^{3+} and Na$_2$SiF$_6$:0.03Eu^{3+}–0.07Tb^{3+}–0.07Ce^{3+} materials) annealed at 400 °C for 2 h

temperature continues to rise, in the temperature range of 600–700 °C, the DSC curve shows an obvious endothermic peak. Combined with Fig. S1, we speculate that this is related to the change in the crystal structure of NaF. That is NaF (JCPDS no. 36–1455) is further converted to NaF (JCPDS no. 01–1184). Since the synthesized Na$_2$SiF$_6$ material starts to decompose from 500 °C, the materials are all annealed at 400 °C for subsequent investigation.

Figure 2 shows representative XRD patterns of the Na$_2$SiF$_6$:xRe^{3+} materials (i.e., Na$_2$SiF$_6$, Na$_2$SiF$_6$:0.07Eu^{3+}, Na$_2$SiF$_6$:0.09Tb^{3+}, Na$_2$SiF$_6$:0.07Ce^{3+} and Na$_2$SiF$_6$:0.03Eu^{3+}–0.07Tb^{3+}–0.07Ce^{3+} materials) annealed

at 400 °C for 2 h. In the figure, all the diffraction peaks of the representative materials correspond well to the hexagonal phase of Na$_2$SiF$_6$ (JCPDS no. 33–1280). There are no other impurity peaks detected from the secondary phase. The result clearly shows that a small amounts of Eu^{3+}, Tb^{3+}, Ce^{3+} doping does not cause significant changes in the matrix lattice in this experiment, and the Eu^{3+}, Tb^{3+}, Ce^{3+} were completely doped into the Na$_2$SiF$_6$ main matrix by replacing the Na$^+$.

According to previous reports, to form a new solid solution, the difference in radius percentage (Dr) between the dopant and the possible substituted ion should not exceed 15%. It can be expressed as [15, 16]: $Dr = \left| \frac{R_1 - R_2}{R_1} \right| \times 100\%$ (where R_1 is the ionic radius of the bulk cation and R_2 is the ionic radius of the dopant). The ionic radius of R_1 (Na$^+$) in the main matrix is 0.97 Å, and the ionic radii of the dopants R_2 (Eu^{3+}), R_2 (Tb^{3+}) and R_2 (Ce^{3+}) are 0.92 Å, 0.95 Å and 1.03 Å, respectively. The calculated Dr (Na$^+$/Eu^{3+}) is about 5.15%, Dr (Na$^+$/Tb^{3+}) is about 2.06%, and Dr (Na$^+$/Ce^{3+}) is about 6.19%, both less than 15%. Compared with Eu^{3+} and Tb^{3+}, Ce^{3+} is more difficult to replace Na$^+$. But from the perspective of the electronegativity of the element, the electronegativity of Na is 0.9, and the electronegativity of Ce is 1.12, which are relatively close. Therefore, these are all confirmed that Eu^{3+}, Tb^{3+} and Ce^{3+} can occupy the Na$^+$ position in the Na$_2$SiF$_6$ host lattice.

Due to the difference in the radii of Eu^{3+}, Tb^{3+}, Ce^{3+} and Na$^+$, the diffraction peaks of the XRD patterns shift with the increase of the contents of Eu^{3+}, Tb^{3+} and Ce^{3+}. The shift can be explained by the Bragg diffraction equation [17]: $2d\sin(\theta) = n\lambda$. When Eu^{3+} (0.92 Å) replaces Na$^+$ (0.97 Å), the d value of the interplanar spacing decreases. To

keep $n\lambda$ constant, the diffraction peaks shift toward the high angle. As the concentration of Eu^{3+} increases, the angle of the offset increases. The phenomenon can be seen in Fig. S2. When Tb^{3+} (0.95 Å) replaces Na^+ (0.97 Å), the same phenomenon can be discovered in Fig. S3. When Ce^{3+} (1.03 Å) replaces Na^+ (0.97 Å), the d value of the interplanar spacing increases, and the diffraction peaks shift toward the low angle. As the concentration of Ce^{3+} increases, the angle of the offset increases (Fig. S4).

Figure S5 shows representative IR spectra of the $Na_2SiF_6{:}xRe^{3+}$ materials (i.e., $Na_2SiF_6{:}0.07Eu^{3+}$, $Na_2SiF_6{:}0.09Tb^{3+}$, $Na_2SiF_6{:}0.07Ce^{3+}$ and $Na_2SiF_6{:}0.03Eu^{3+}$–$0.07Tb^{3+}$–$0.07Ce^{3+}$ materials) annealed at 400 °C for 2 h. In the figure, the absorption peak at 475 cm^{-1} corresponds to the bending vibration of SiF_6^{2-}.

The absorption peaks at 730 cm^{-1} and 495 cm^{-1} correspond to the tensile vibration of SiF_6^{2-} [18]. This is consistent with XRD analysis, so the materials are pure hexagonal Na_2SiF_6. In addition, according to previous reports [19], the characteristic peak appearing at 1102 cm^{-1} is caused by the exchange of bromide ion with fluoride ion in sodium fluorosilicate.

Figure 3a shows representative TEM image of the $Na_2SiF_6{:}0.03Eu^{3+}$–$0.07Tb^{3+}$–$0.07Ce^{3+}$ material. It can be seen that the material is mainly made up of circular particles, which are prone to agglomeration. And the size of the crystal particle obtained by particle size measurement is about 119.15 nm. Figure 3b, c shows the electron diffraction pattern and HRTEM image of the $Na_2SiF_6{:}0.03Eu^{3+}$–$0.07Tb^{3+}$–$0.07Ce^{3+}$ material. The figures show diffraction spots or rings and clear lattice fringes,

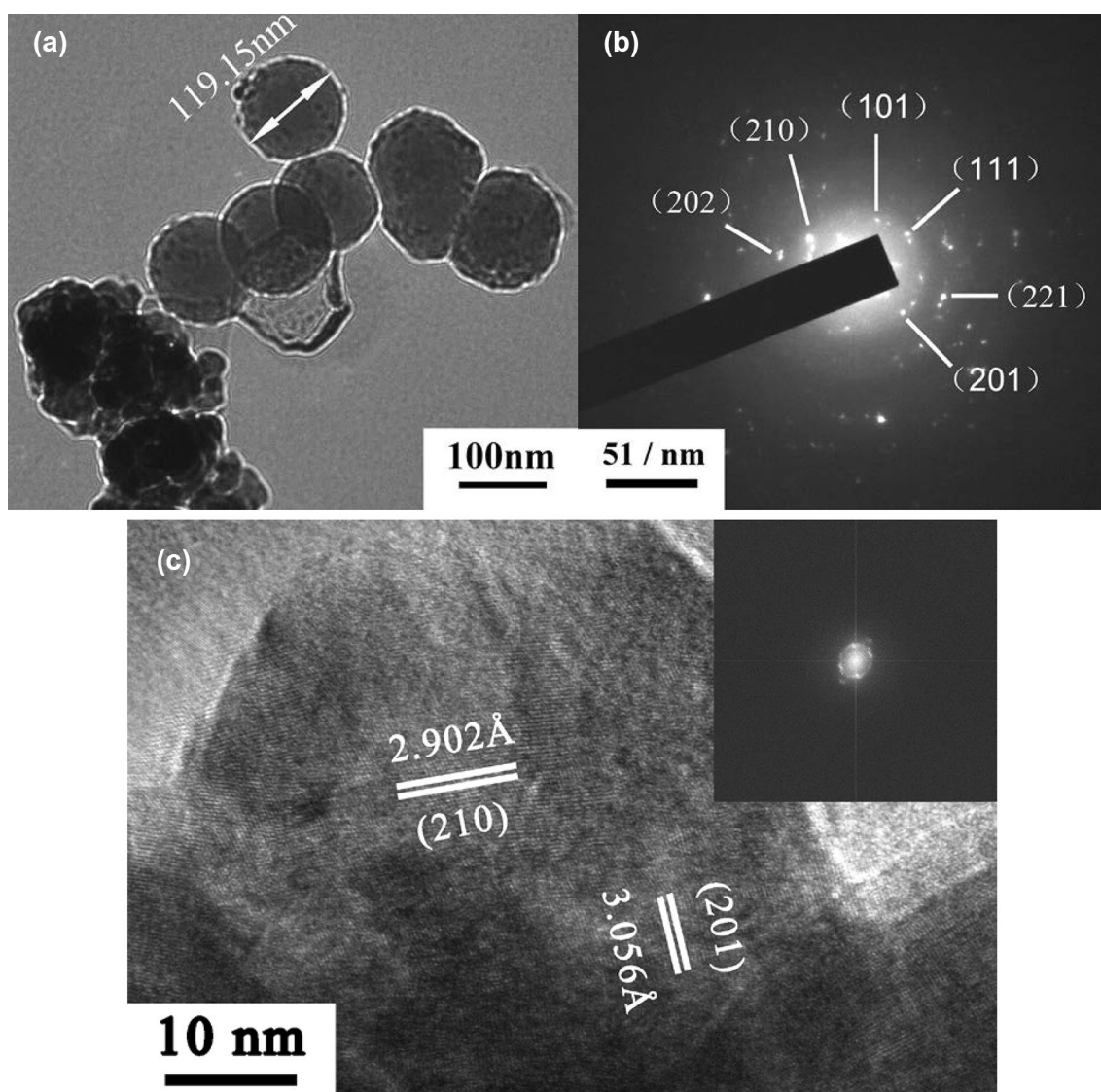**Fig. 3** Representative TEM image (**a**) electron diffraction pattern (**b**) and HRTEM image **c** of the $Na_2SiF_6{:}0.03Eu^{3+}$–$0.07Tb^{3+}$–$0.07Ce^{3+}$ material

from which the (210), (201) and other facets of hexagonal phase Na$_2$SiF$_6$ could be clearly discerned. These lattice spacings are consistent with the Na$_2$SiF$_6$ (JCPDS no. 33–1280) measured by XRD. They further evidence that the material has good crystallinity.

Figure 4 shows the representative EDS energy spectrum of the Na$_2$SiF$_6$:0.03Eu^{3+}–0.07Tb^{3+}–0.07Ce^{3+} material. O, F, Na, Si, S, Eu, Tb, and Ce elements can be observed in the energy spectrum. And the elemental ratios of Eu, Tb and Ce show that the three ions are uniformly distributed in the whole particle range according to the known quantity, indicating the formation of the Na$_2$SiF$_6$:0.03Eu^{3+}–0.07Tb^{3+}–0.07Ce^{3+} material.

Figure S6 shows the representative Raman spectroscopy of the Na$_2$SiF$_6$ and Na$_2$SiF$_6$:0.03Eu^{3+}–0.07Tb^{3+}–0.07Ce^{3+} materials. According to previous reports [20–22], Raman scattering is sensitive to even symmetry (gerade) modes of vibration, while infrared radiation is sensitive to odd (ungerade) modes. There are a total of six phonon modes in the octahedral crystal field. Three gerade modes (v_1, v_2 and v_5) are Raman active, while the remaining ungerade modes are IR active (v_3 and v_4) and silent modes (v_6). However, in highly defective crystalline materials, the parity selection rules for Raman scattering may be partially relaxed or significantly changed. As this time, some inhibition modes can become Raman active, and even new local vibration modes can be observed. Therefore, if Eu^{3+}, Tb^{3+}, Ce^{3+} doped Na$_2$SiF$_6$:0.03Eu^{3+}–0.07Tb^{3+}–0.07Ce^{3+} material presences highly defective, then some of the original inhibition modes and the new local vibration modes should be observed in the figure. However, it can be seen from the figure that the vibration peak positions of the two materials are identical. The result clearly shows that the as-synthesized Na$_2$SiF$_6$:0.03Eu^{3+}–0.07Tb^{3+}–0.07Ce^{3+} materials have pure hexagonal phase.

3.2 Luminescence performance analysis of the Na$_2$SiF$_6$:xRe^{3+} (Re^{3+} = Eu^{3+}, Tb^{3+}, Ce^{3+}) materials

3.2.1 Luminescence performance of the Na$_2$SiF$_6$:xEu^{3+} materials

Figure 5a shows excitation and emission spectra of a representative material Na$_2$SiF$_6$:0.07Eu^{3+} in the Na$_2$SiF$_6$:xEu^{3+} materials. In the excitation spectrum, a series of the sharp absorption peaks in the range of 300–500 nm are caused by the 4f internal transitions of Eu^{3+}. That is, the excitation peaks at 318, 362, 381, 395, 415, and 465 nm are attributed to $^7F_0 \rightarrow {}^5H_6$, $^7F_0 \rightarrow {}^5D_4$, $^7F_0 \rightarrow {}^5G_2$, $^7F_0 \rightarrow {}^5L_6$, $^7F_0 \rightarrow {}^5D_3$ and $^7F_0 \rightarrow {}^5D_2$ transitions of Eu^{3+} [23, 24], respectively. Among them, the shape of the excitation
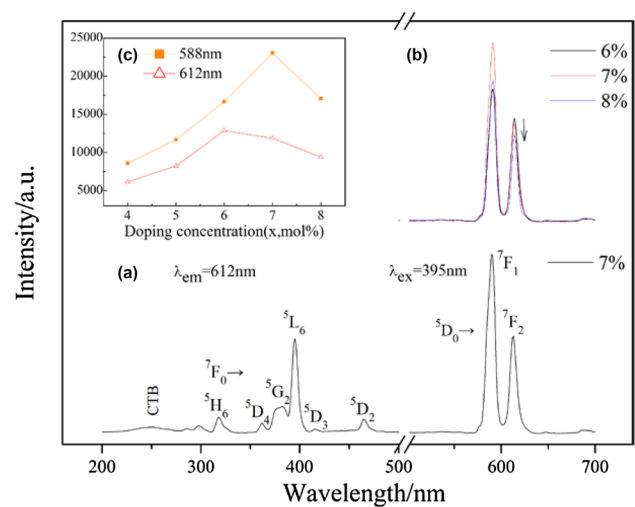
Fig. 5 Excitation and emission spectra of the Na$_2$SiF$_6$:0.07Eu^{3+} material (a) emission spectra of the Na$_2$SiF$_6$:xEu^{3+} (x = 6–8 mol%) materials (b) and emission intensity spectra of the Na$_2$SiF$_6$:xEu^{3+} materials with different Eu^{3+} concentrations (c)
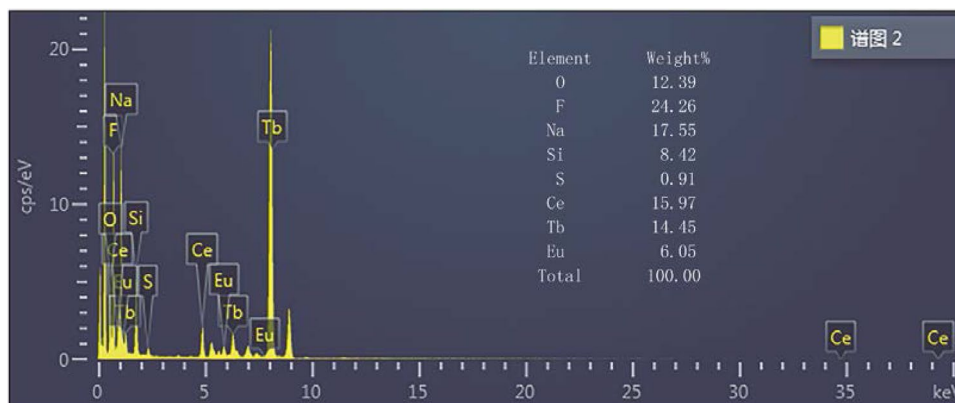
Fig. 4 Representative EDS energy spectrum of the Na$_2$SiF$_6$:0.03Eu^{3+}–0.07Tb^{3+}–0.07Ce^{3+} material

peak located at 395 nm in the ultraviolet region is the sharpest and the peak intensity is the strongest. That is, the excitation efficiency of this wavelength is high, so it is selected as the optimal excitation wavelength. In addition, the Na_2SiF_6:0.07Eu^{3+} material has a very weak single absorption broadband in the ultraviolet short-wave region (200–290 nm), which is caused by the charge transfer band of Eu^{3+}–O^{2-}. When Eu^{3+} is substituted for Na^+, a positively charged $Eu^{..}Na$ vacancy defect is generated. It requires charge compensation. In atmospheric and non-reducing atmospheres, the two F^- may enter the gap in a gap-filled manner to achieve charge balance. At the same time, trace oxygen in the atmosphere or other sources of oxygen in the system may also replace F^-, thereby achieving charge compensation. That is, in the Na_2SiF_6 lattice, Eu^{3+} combines with the nearest trace O^{2-} and the next adjacent Na^+ to form Eu^{3+}–O^{2-}–Na^+. And the electrons of O^{2-} migrate from its full 2p orbit to the partially filled 4f^6 shell of Eu^{3+}, resulting in a weak charge transfer band [25].

In the emission spectrum, the Na_2SiF_6:0.07Eu^{3+} material under the excitation of 395 nm shows characteristic emission peaks of Eu^{3+} at 588 nm ($^5D_0 \rightarrow {}^7F_1$) and 612 nm ($^5D_0 \rightarrow {}^7F_2$), respectively. The strongest radiation of the Eu^{3+} in the emission spectrum mainly depends on its symmetry of the occupied position in the lattice of the matrix. When the symmetry is low, the strongest radiation appears as an electric dipole transition ($^5D_0 \rightarrow {}^7F_2$), otherwise it appears as a magnetic dipole transition ($^5D_0 \rightarrow {}^7F_1$) [26]. In the Na_2SiF_6 matrix, the emission of Eu^{3+} mainly manifests as a magnetic dipole transition ($^5D_0 \rightarrow {}^7F_1$) at 588 nm. This is because in the Na_2SiF_6 crystal, Eu^{3+} mainly replaces the position of Na^+. And Na^+ occupies a highly symmetry position in the Na_2SiF_6 lattice. So the emission of Eu^{3+} is dominated by the magnetic dipole transition ($^5D_0 \rightarrow {}^7F_1$) at 588 nm [27]. The characteristic emission peak of Eu^{3+} at 612 nm is the electric dipole transition ($^5D_0 \rightarrow {}^7F_2$). According to the selection rule, this electric dipole transition of $\Delta l = 0$ was originally forbidden [28]. However, as for the Na_2SiF_6:$x$$Eu^{3+}$ ($x = 6$–8 mol%) materials in Fig. 5b, when the doping amount of Eu^{3+} is 6 mol%, the original forbidden transition is relatively strong. This is mainly due to the fact that the 4f configuration is mixed with the oppositely symmetric configuration g or d, or the symmetry deviates from the inversion center, so that the original forbidden f–f transition becomes permissible. It indicates that Eu^{3+} is located in the center of the asymmetric field in the Na_2SiF_6 lattice at this time, presumably due to the partial Eu^{3+} entering the lattice gap. But as the concentration of Eu^{3+} increases, this transition gradually diminishes. This is because in the Na_2SiF_6 lattice, Eu^{3+} mainly replaces the Na^+ position, and the Eu^{3+} (0.92 Å) radius is smaller than the Na^+ (0.97 Å) radius. Therefore, as the concentration of Eu^{3+} increases,

the Na_2SiF_6 unit cell shrinks and the crystal field effect is enhanced [27], making it more difficult for Eu^{3+} to enter the lattice gap.

Figure 5c shows emission intensity spectra of Na_2SiF_6:$x$$Eu^{3+}$ materials with different Eu^{3+} concentrations. It can be seen that as the Eu^{3+} doping amount increases, the luminescence intensity of the material increases, reaching a maximum at 7 mol% Eu^{3+}. At this time, the energy transfer rate between the luminescent centers of Eu^{3+} is equal to the emission rate, so the luminescence reaches the strongest. As the doping amount continues to increase, the luminescence is weakened. This is because the positions between Eu^{3+} are close to each other, and the activator ions in the excited state interact with each other, thereby increasing the new energy loss mechanism, and resulting in concentration quenching phenomenon [29].

3.2.2 Luminescence performance of the Na_2SiF_6:$y$$Tb^{3+}$ materials

Figure 6a shows excitation and emission spectra of a representative material Na_2SiF_6:0.09Tb^{3+} in the Na_2SiF_6:$y$$Tb^{3+}$ materials. In the excitation spectrum, with the wavelength range of 220–250 nm, the broadband centered at 230, 265 nm all belong to the $4f^8 \rightarrow 4f^7 5d^1$ transition of Tb^{3+}. The narrow peaks at 285, 303, 318, 342, and 352 nm correspond to $^7F_6 \rightarrow {}^3H_3$, $^7F_6 \rightarrow {}^5H_6$, $^7F_6 \rightarrow {}^5H_7$, $^7F_6 \rightarrow {}^5L_7$ and $^7F_6 \rightarrow {}^5D_2$ transitions of Tb^{3+} [30, 31], respectively. The characteristic excitation peaks at 370 and 378 nm correspond to the $^7F_6 \rightarrow {}^5L_{10}$ transition of Tb^{3+}. The reason why the excitation peak generated by this transition splits into two peaks is as follows: the 5d electrons are in the outer electron orbit, which are greatly affected by environmental factors, and the $^7F_6$ energy level degenerate releases, causing the stokes splitting and forming two lines [27, 28]. Among these excitation bands, the excitation band at 378 nm in the ultraviolet region has the highest intensity, so it is selected as the optimum excitation wavelength. In the emission spectrum, the Na_2SiF_6:0.09Tb^{3+} material under the excitation of 378 nm has a series of sharp emission peaks at 492, 544, 592 and 612 nm, corresponding to $^5D_4 \rightarrow {}^7F_J$ ($J = 6, 5, 4, 3$) transitions of Tb^{3+} [32, 33].

Figure 6a shows the simplified energy levels image of Tb^{3+} and emission spectra of the Na_2SiF_6:0.09Tb^{3+} material under the excitations of 352, 370 and 378 nm. Under the excitation of 378 nm, electrons first are excited from the ground state of $^7F_6$ to the excited state of $^5L_{10}$. Then, a non-radiative transition occurs, transitioning to a lower excited state at the $^5D_3$ level. Subsequently, a second non-radiative transition occurs, causing the electrons decay from the $^5D_3$ level to the $^5D_4$ level. Finally, a radiation transition occurs, resulting in a series of characteristic emissions of Tb^{3+}, namely $^5D_4 \rightarrow {}^7F_6$ at 492 nm, $^5D_4 \rightarrow {}^7F_5$ at 544 nm,

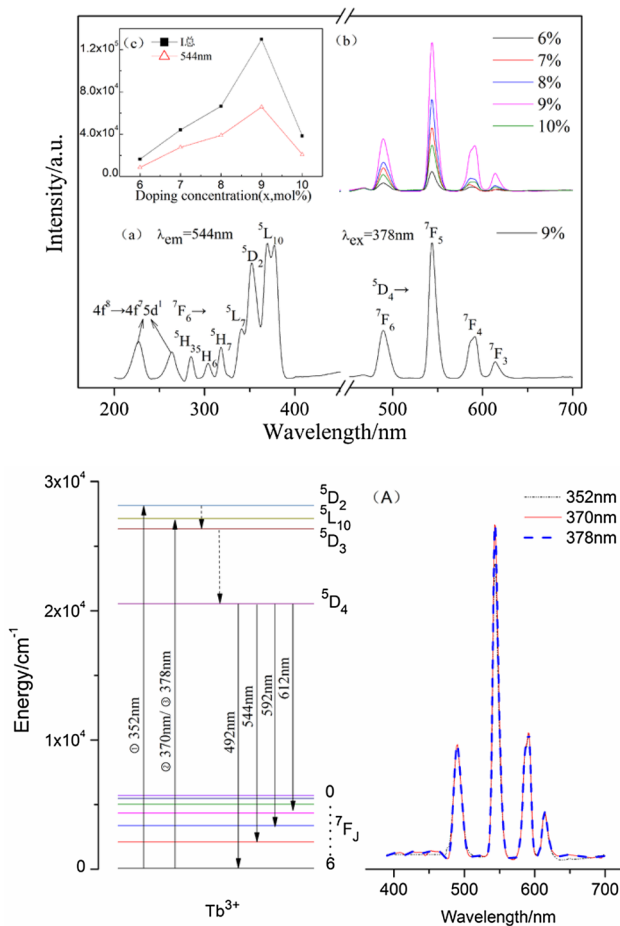**Fig. 6** Excitation and emission spectra of the Na₂SiF₆:0.09Tb³⁺ material (a) emission spectra of the Na₂SiF₆:yTb³⁺(y=6–10 mol%) materials (b) emission intensity spectra of the Na₂SiF₆:yTb³⁺ materials with different Tb³⁺ concentrations (c) simplified energy levels image of Tb³⁺ and emission spectra of the Na₂SiF₆:0.09Tb³⁺ material under the excitations of 352, 370 and 378 nm (A)

Fig. 7 Excitation and emission spectra of the Na₂SiF₆:0.07Ce³⁺ material (a) and emission intensity spectra of the Na₂SiF₆:zCe³⁺ materials with different Ce³⁺ concentrations (b)

$^5D_4 \rightarrow {}^7F_4$ at 592 nm, and $^5D_4 \rightarrow {}^7F_3$ at 612 nm [34]. Further, using excitations of 352 nm and 370 nm as excitation wavelengths respectively, almost the same emission spectrums are obtained. And the energy level transitions of the emission process are also almost same. That means, the illumination mechanisms are the same.

Figure 6b, c is emission spectrum and emission intensity spectra of the Na₂SiF₆:yTb³⁺ materials with different Tb³⁺ concentrations, respectively. The combination of the two graphs shows that the different Tb³⁺ doping amounts have little effect on the distribution position of the emission peaks, but the intensity of each emission peak greatly changes with the increase of Tb³⁺ doping amount. It is obvious that as the Tb³⁺ doping amount increases, the luminescence intensity of the material increases, reaching a maximum at 9 mol% Tb³⁺. However, since the non-radiative energy transfer between adjacent Tb³⁺ causes concentration
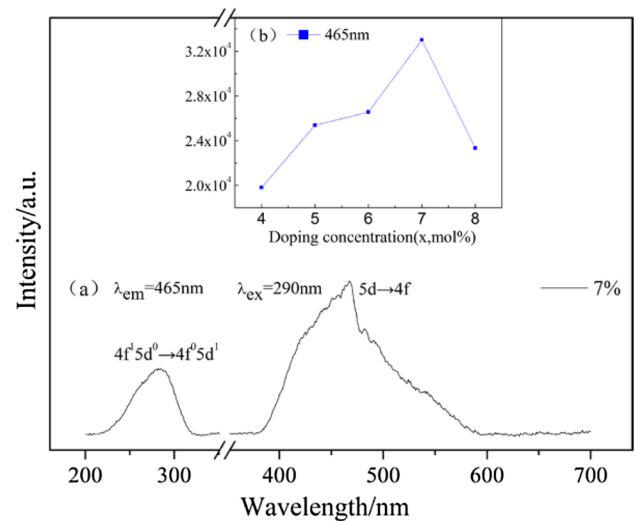
quenching, the luminescence intensity of the material begins to decrease as the increasing of the concentration of Tb³⁺. Non-radiative energy transfer between activators is achieved primarily through two mechanisms: exchange interaction and multipole–multipole interaction. In general, when the critical distance between activator ions is less than 5 Å (ie, $R_c < 5$ Å), the non-radiative energy transfer between activators is dominated by exchange interactions. When $R_c > 5$ Å, the multipole–multipole interaction is dominant. Therefore, to explore the concentration quenching mechanism of Tb³⁺ in this system, the critical distance R_c between Tb³⁺ in the Na₂SiF₆ matrix is calculated by the given formula [35, 36]: $R_c = 2\left(\frac{3V}{4\pi Z X_c}\right)^{1/3}$ (where V is the volume of the unit cell, Z is the number of cations per unit cell, and X_c is the critical doping concentration of the activator ion). For the Na₂SiF₆:yTb³⁺ materials, $V = 195.41 Å^3$, $Z = 3$, X_c (Tb³⁺) = 9 mol%. So the calculated R_c (Tb³⁺) is about 11.14 Å, which is much larger than 5 Å. Therefore, the multipole–multipole interaction is the main mechanism for the concentration quenching of Tb³⁺ in this system.

3.2.3 Luminescence performance of the Na₂SiF₆:zCe³⁺ materials

Figure 7a shows excitation and emission spectra of a representative material Na₂SiF₆:0.07Ce³⁺ in the Na₂SiF₆:zCe³⁺ materials. In the excitation spectrum, there is a broad and strong excitation band from 210 to 310 nm, centered at about 290 nm, so selecting 290 nm of the ultraviolet light as the optimal excitation wavelength. The peak is assigned to the $4f \rightarrow 5d$ transition of Ce³⁺. In the emission spectrum, it has a

single-peak broadband in the range of 380–600 nm, centered at about 465 nm, due to the $5d \rightarrow 4f$ transition of Ce^{3+}. Its ground state is $4f^1 5d^0$ and the excited state is $4f^0 5d^1$. When $4f$ loses electrons, it leaves two energy levels of $^2F_{7/2}$ and $^2F_{5/2}$, and the energy difference between the two levels is about 2300 cm^{-1}. At this time, the $5d$ electrons in the excited state will form a 2D energy level, and the 2D energy level will further split into two energy levels of $^2D_{3/2}$ and $^2D_{5/2}$ due to spin–orbit coupling. The energy difference between the two energy levels is about 1890 cm^{-1}. The $5d$ orbit of Ce^{3+} is exposed to the outer layer. When it is subjected to the crystal field, the original discrete energy levels will form continuous energy bands. Further, when a $5d \rightarrow 4f$ energy level transition occurs, a luminescence phenomenon occurs in the visible light region [37].

Figure 7b shows emission intensity spectra of $Na_2SiF_6{:}zCe^{3+}$ materials with different Ce^{3+} concentrations. It is obvious that as the Ce^{3+} doping amount increases, the luminescence intensity of the material increases, reaching a maximum at 7 mol% Ce^{3+}. And when the doping amount continues to increase, the luminescence intensity begins to decrease, and the concentration quenching phenomenon also occurs.

Based on the above analyses, it can be clearly seen that the Eu^{3+}, Tb^{3+} and Ce^{3+} single-doped $Na_2SiF_6{:}xRe^{3+}$ materials can illuminate red, green and blue primary colors under specific UV light excitation. Figure 8 shows the CIE coordinates of $Na_2SiF_6{:}0.07Eu^{3+}$, $Na_2SiF_6{:}0.09Tb^{3+}$ and
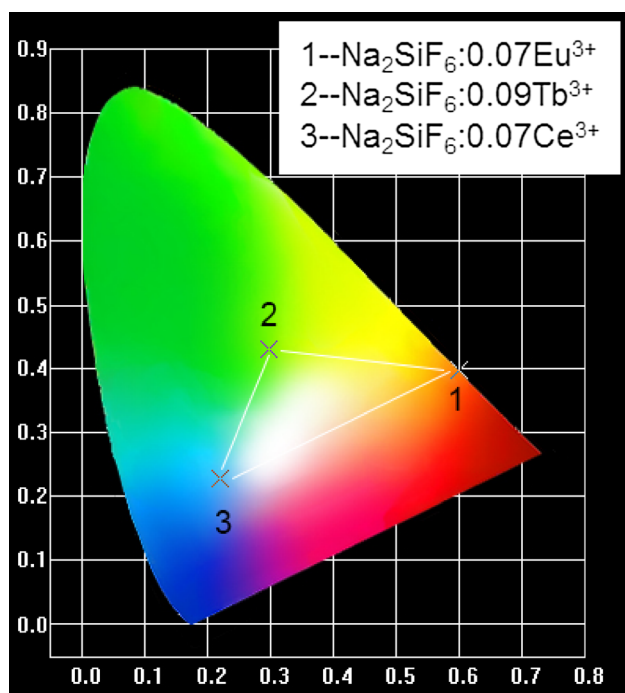
$Na_2SiF_6{:}0.07Ce^{3+}$ materials, and their color coordinates are listed in Table 1. In the figure, serial numbers 1, 2 and 3 correspond to the red, green and blue CIE coordinates of $Na_2SiF_6{:}0.07Eu^{3+}$ ($\lambda_{ex} = 395$ nm), $Na_2SiF_6{:}0.09Tb^{3+}$ ($\lambda_{ex} = 378$ nm) and $Na_2SiF_6{:}0.07Ce^{3+}$ ($\lambda_{ex} = 290$ nm), respectively. The triangle in the figure depicts the tunable regions of the Eu^{3+}, Tb^{3+} and Ce^{3+} single-doping materials. To obtain a single-component white phosphor, Eu^{3+}, Tb^{3+} and Ce^{3+} are further co-doped in the Na_2SiF_6 matrix. The following is a detailed discussion of the luminescence performance of the three-doped system, namely the $Na_2SiF_6{:}0.03Eu^{3+}$–$0.07Tb^{3+}$–$0.07Ce^{3+}$ material.

3.2.4 Luminescence performance of the $Na_2SiF_6{:}0.03Eu^{3+}$– $0.07Tb^{3+}$–$0.07Ce^{3+}$ material

Selecting the red emission wavelength (612 nm) of Eu^{3+} as the monitoring wavelength, the measured excitation spectra of the $Na_2SiF_6{:}0.03Eu^{3+}$–$0.07Tb^{3+}$–$0.07Ce^{3+}$ material are shown in Fig. 9a. The broadband at 290 nm belongs to the $4f \rightarrow 5d$ electronic transition of Ce^{3+}. The sharp excitation peaks at 318, 352, 378, and 395 nm correspond to $^7F_0 \rightarrow {^5H_6}$ of Eu^{3+} or $^7F_6 \rightarrow {^5H_7}$ of Tb^{3+}, $^7F_6 \rightarrow {^5D_2}$ of Tb^{3+}, $^7F_6 \rightarrow {^5L_{10}}$ of Tb^{3+} and $^7F_0 \rightarrow {^5L_6}$ of Eu^{3+} [38, 39]. According to various excitation characteristics, the measured material exhibits multi-peak emission in the visible light region by selecting the above-monitored different excitation wavelengths as excited wavelengths in turn. Figure 9b shows emission spectrum of the $Na_2SiF_6{:}0.03Eu^{3+}$–$0.07Tb^{3+}$–$0.07Ce^{3+}$ material excited by 290 nm. It can be seen that the main emission peaks are located at 465, 490, 544, 588 and 612 nm, respectively. The spectrum represents full-color emission, including red, green and blue components that allow the realization of white light emitting. Among them, the emission peak at 465 nm corresponds to the $5d \rightarrow 4f$ transition of Ce^{3+} and the $^5D_2 \rightarrow {^7F_0}$ transition of Eu^{3+}. Several peaks at 490, 544, and 588 nm are attributed to the $^5D_4 \rightarrow {^7F_J}$ ($J = 6$, 5, 4) transitions of Tb^{3+}, respectively. In addition, Tb^{3+} can also produce weak red emission at 612 nm ($^5D_4 \rightarrow {^7F_3}$), while red emission at 588 and 612 nm is attributed to the $^5D_0 \rightarrow {^7F_J}$ ($J = 1$, 2) transitions of Eu^{3+}, respectively [40]. Therefore, there is a superposition of the emission spectra of Tb^{3+} and Eu^{3+} in the red light-emitting region of 590–620 nm. Figure S7 is the quantum yield diagram of the

Fig. 8 CIE coordinates of the $Na_2SiF_6{:}0.07Eu^{3+}$, $Na_2SiF_6{:}0.09Tb^{3+}$ and $Na_2SiF_6{:}0.07Ce^{3+}$ materials

Table 1 Color coordinates of the $Na_2SiF_6{:}0.07Eu^{3+}$, $Na_2SiF_6{:}0.09Tb^{3+}$ and $Na_2SiF_6{:}0.07Ce^{3+}$ materials

Re^{3+}	x	y
Eu^{3+}	0.6008	0.3987
Tb^{3+}	0.2983	0.4300
Ce^{3+}	0.2195	0.2264

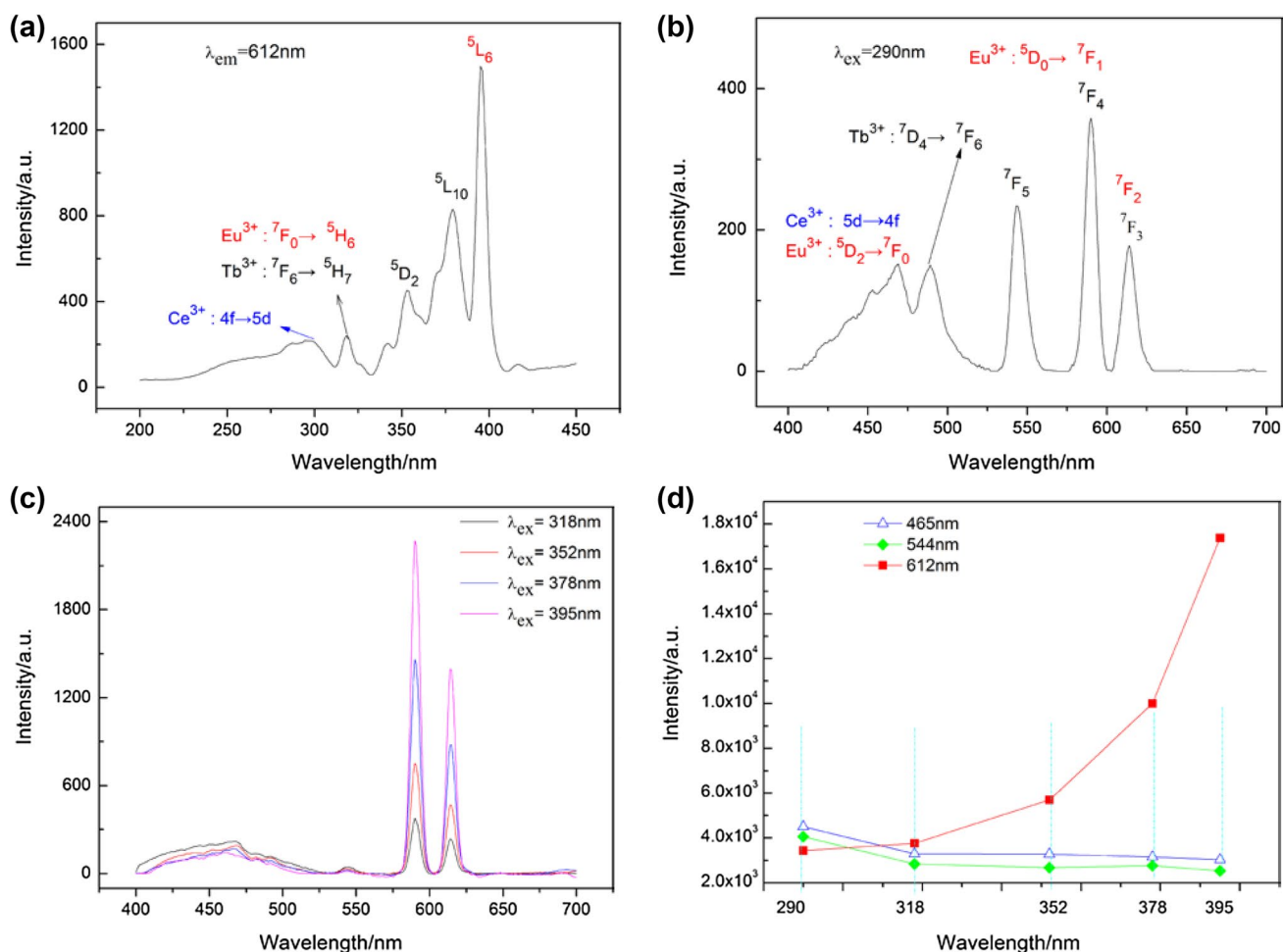**Fig. 9** The Na$_2$SiF$_6$:0.03Eu^{3+}–0.07Tb^{3+}–0.07Ce^{3+} material's excitation spectra (**a**) emission spectra under the excitation of 290 nm (**b**) emission spectra under the excitation of different excitation wavelengths (**c**) and emission intensity spectra of main characteristic peaks corresponding to red, green and blue (**d**)

Na$_2$SiF$_6$:0.03Eu^{3+}–0.07Tb^{3+}–0.07Ce^{3+} material excited by 290 nm, and the result is 4.92%.

Figure 9c shows emission spectra of the Na$_2$SiF$_6$:0.03Eu^{3+}–0.07Tb^{3+}–0.07Ce^{3+} material excited by different excitation wavelengths. It can be seen that the Na$_2$SiF$_6$:0.03Eu^{3+}–0.07Tb^{3+}–0.07Ce^{3+} material can all detect the red characteristic luminescence of Eu^{3+}, the green characteristic luminescence of Tb^{3+} and the blue characteristic luminescence from Ce^{3+} under the excitation of UV light with different excitation wavelengths. However, the luminescence intensity of each emission peak varies depending on the energy of the excitation wavelength [41, 42]. As the excitation wavelength energy decreases, the emission peak intensity of Ce^{3+} at 465 nm decreases, and the emission peak intensity of Tb^{3+} at 544 nm also decreases slightly, but the emission peak intensity of Eu^{3+} at 612 nm is rapidly enhanced. The change in their energy is shown in Fig. 9d. From these adjustable emission spectra, it can know that the intensity of emission of each characteristic emitted light

from the same phosphor can be adjusted by changing the excitation wavelength of the UV light.

Figure 10 shows simplified energy level diagram of Ce^{3+}, Tb^{3+} and Eu^{3+} of the Na$_2$SiF$_6$:0.03Eu^{3+}–0.07Tb^{3+}–0.07Ce^{3+} material to explain possible energy transfer during excitation and emission. In the Na$_2$SiF$_6$:zCe^{3+} materials, Ce^{3+} replaces the Na$^+$ level. So it is speculated that in the Na$_2$SiF$_6$:0.03Eu^{3+}–0.07Tb^{3+}–0.07Ce^{3+} material, Ce^{3+} still replaces the Na$^+$ level. Since Na$^+$ is in the six-coordinate field of the Na$_2$SiF$_6$ matrix [22], the 5d orbit of Ce^{3+} is still in the six-coordinate field after replacing Na$^+$. In addition, since the multi-doping is easy to cause lattice distortion, it is speculated that the 5d orbit of Ce^{3+} is in the twisted six-coordinate field. At this time, the 5d orbit is prone to splitting. So the two d-orbits of the energy reduction of Ce^{3+} calculated by combing the excitation and emission spectrum are located at 34,040 and 22,499 cm^{-1}, respectively [43].

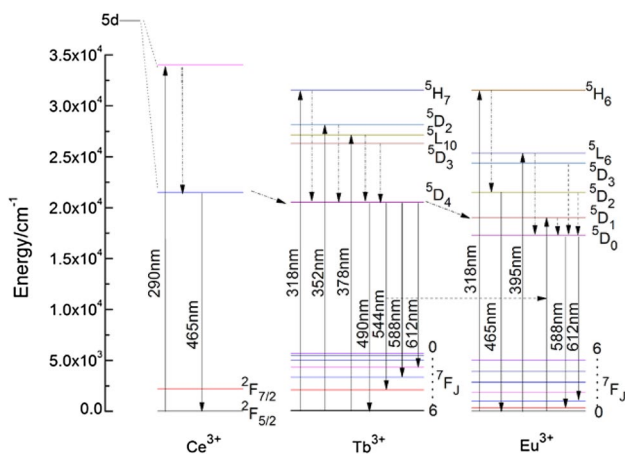Based on the above experimental results, it is considered that the following luminescence processes exist in the

Fig. 10 Simplified energy level diagram of Ce^{3+}, Tb^{3+} and Eu^{3+} of the Na_2SiF_6:$0.03Eu^{3+}$–$0.07Tb^{3+}$–$0.07Ce^{3+}$ material

Na_2SiF_6:$0.03Eu^{3+}$–$0.07Tb^{3+}$–$0.07Ce^{3+}$ material. Under the excitation of 290 nm ultraviolet light, electrons on Ce^{3+} are transited from the ground state level to the splitting higher $5d$ energy level (34,040 cm^{-1}). Then these electrons relax to a lower $5d$ energy level (22,499 cm^{-1}) through multi-phonon relaxation, and further produce the characteristic emissions of Ce^{3+}. Or these electrons transfer their excitation energy from the lower $5d$ energy level (22,499 cm^{-1}) of Ce^{3+} to the excited $^5D_4$ energy level of Tb^{3+} by cross relaxation, and further generate the characteristic emissions of Tb^{3+}. Or these electrons transfer their excitation energy to the $^5D_1$ level of Eu^{3+} via Tb^{3+} bridging, then relax to the $^5D_1$ level of Eu^{3+} through multi-phonon relaxation, and further yield the characteristic emissions of Eu^{3+} [44–46].

Since the energy difference between $^5D_4 \rightarrow {}^7F_5$ of Tb^{3+} is similar to that of $^7F_0 \rightarrow {}^5D_1$ of Eu^{3+}, the energy released

by $^5D_4 \rightarrow {}^7F_5$ of Tb^{3+} in the system is transmitted to the $^7F_0 \rightarrow {}^5D_1$ of Eu^{3+} in the form of non-radiative resonance transmission. Then these electrons relax to the lowest excited $^5D_0$ level of Eu^{3+} by multi-phonon relaxation, and further the characteristic emissions of Eu^{3+} occur [8, 47]. As the excitation wavelength increases and the excitation energy decreases, the characteristic emissions corresponding to Ce^{3+} and Tb^{3+} requiring higher excitation energy are gradually weakened, while the characteristic emissions for Eu^{3+} requiring lower excitation energy is continuously enhanced. When the optimal excitation wavelength (395 nm) of Eu^{3+} is selected for excitation, emission spectrum of the material reflects the strongest characteristic emission of Eu^{3+}.

Figure 11a shows the emission spectrum of Na_2SiF_6:$0.07Ce^{3+}$ ($\lambda_{ex} = 290$ nm) material and the excitation spectrum of Na_2SiF_6:$0.07Tb^{3+}$ ($\lambda_{em} = 542$ nm) material. The spectral overlap is observed between the emission spectrum of Ce^{3+} and the excitation spectrum of Tb^{3+}. It is known from Dexter's energy transfer theory [48, 49] that there is a possibility of the energy transfer from Ce^{3+} to Tb^{3+}. The energy levels and processes involved can be described by $5d$ (Ce^{3+}) + $^7F_5$ (Tb^{3+}) $\rightarrow 4f$ (Ce^3) + $^5D_4$ (Tb^{3+}). Figure 11b shows the emission spectrum of the Na_2SiF_6:$0.07Tb^{3+}$ material and the excitation spectrum of the Na_2SiF_6:$0.03Eu^{3+}$ material. The spectral overlap is also observed between the emission spectrum of Tb^{3+} and the excitation spectrum of Eu^{3+}, indicating that there is also the possibility of the energy transfer from Tb^{3+} to Eu^{3+}. The energy levels and processes involved can be described as $^5D_4$ (Tb^{3+}) + $^7F_2$ (Eu^{3+}) $\rightarrow {}^7F_5$ (Tb^{3+}) + $^5D_0$ (Eu^{3+}). These two phenomena can further support the energy transfer process involved above.

Figure 12 shows CIE coordinates of the Na_2SiF_6:$0.03Eu^{3+}$–$0.07Tb^{3+}$–$0.07Ce^{3+}$ material excited by UV light at different excitation wavelengths, and their
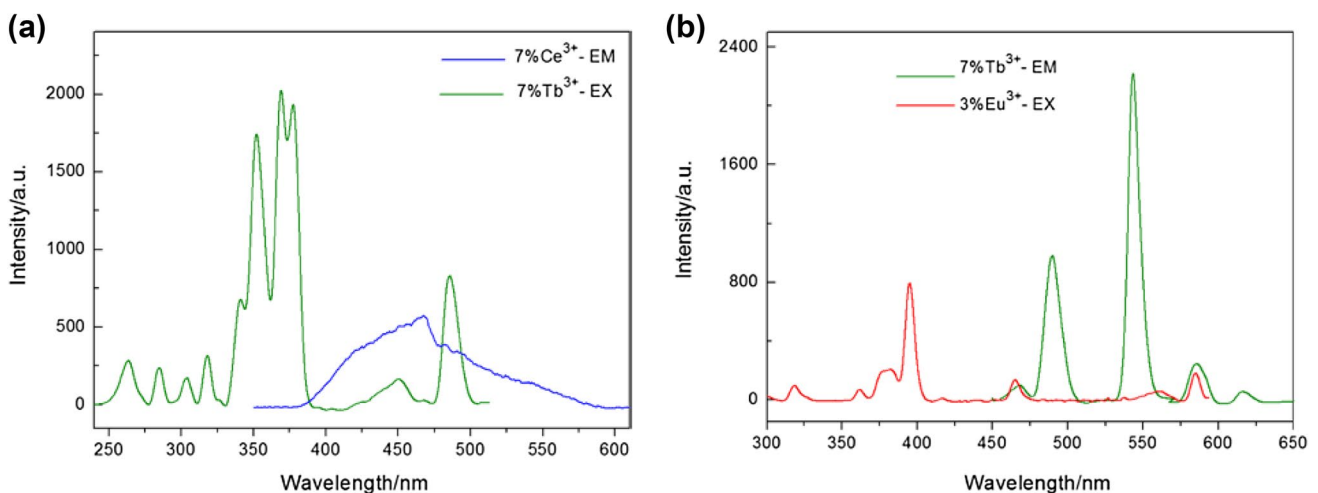

Fig. 11 Emission spectra of the Na_2SiF_6:$0.07Ce^{3+}$ material and excitation spectra of the Na_2SiF_6:$0.07Tb^{3+}$ material (**a**) emission spectra of the Na_2SiF_6:$0.07Tb^{3+}$ material and excitation spectra of the Na_2SiF_6:$0.03Eu^{3+}$ material (**b**)
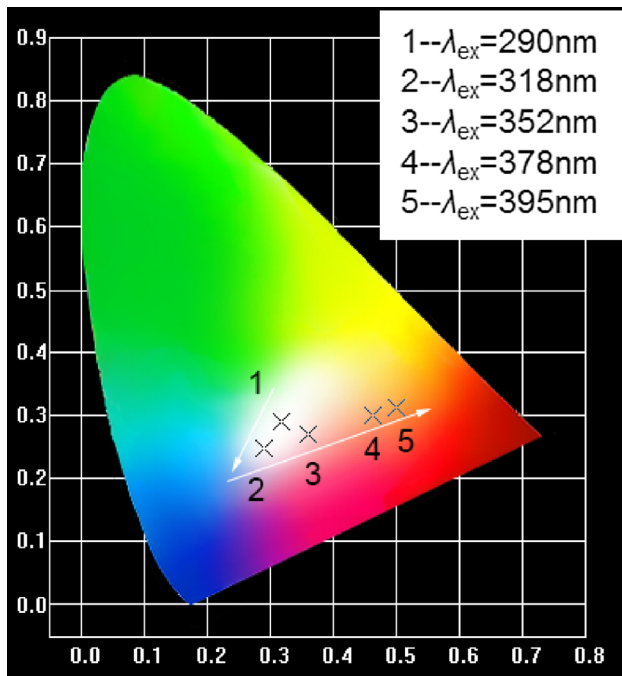
Fig. 12 CIE coordinates of the Na$_2$SiF$_6$:0.03Eu^{3+}–0.07Tb^{3+}–0.07Ce^{3+} material excited by UV light at different excitation wavelengths

Table 2 Color coordinates of the Na$_2$SiF$_6$:0.03Eu^{3+}–0.07Tb^{3+}–0.07Ce^{3+} material excited by UV light at different excitation wavelengths

λ_{ex}/nm	x	y
290	0.3181	0.2892
318	0.2909	0.2465
352	0.3593	0.2692
378	0.4635	0.3012
395	0.4999	0.3122

color coordinates are listed in Table 2. To visually understand the emission color of the material, the chromaticity coordinates of the material under UV light excitation of different excitation wavelengths are marked by numerical serial number in the CIE chromaticity diagram. In the diagram, the elliptical region in the middle belongs to the white light emitting region. And the serial numbers 1, 2, 3, 4, and 5 represent the chromaticity coordinates of the material excited by UV light at 290, 318, 352, 378 and 395 nm, respectively. It can be seen that the emission color of the Na$_2$SiF$_6$:0.03Eu^{3+}–0.07Tb^{3+}–0.07Ce^{3+} material changes from white light to cold white light, warm white light and red orange light as the increase of excitation wavelength. Among them, the luminescence of the material under the excitation of 290 nm is the closest to the ideal white light. The white light excited by 318 nm contains more blue components. The white light excited by 352 nm contains more

red components, and the human eye feels more comfortable with this light. Under the excitation of 378 and 395 nm, the material mainly emits red–orange light. It is concluded that the emission color from the same phosphor can be adjusted by changing the excitation wavelength of the UV light.

4 Conclusions

In this paper, Eu, Tb and Ce mono-doped and ternary co-doped Na$_2$SiF$_6$:xRe^{3+} luminescent materials were synthesized by co-precipitation method, and the structure and luminescence properties of the materials were investigated. The results show that the Eu, Tb and Ce single-doped Na$_2$SiF$_6$:xRe^{3+} materials exhibit characteristic red, green and blue luminescence, respectively, under appropriate UV light excitation. The ternary co-doped material exhibits full-color emission represented by Na$_2$SiF$_6$:0.03Eu^{3+}–0.07Tb^{3+}–0.07Ce^{3+} material and it contains the following luminescence phenomenon. As the excitation wavelength increases and the excitation energy decreases, the characteristic emissions corresponding to Ce^{3+} and Tb^{3+} are gradually weakened, and the characteristic emission corresponding to Eu^{3+} is continuously enhanced. The emission color changes from white light to cold white light, warm white light and red orange light as the increase of excitation wavelength. Among them, the luminescence of the material excited by 290 nm is the closest to the ideal white light. Under the excitation of 395 nm, the luminescence of the material is the strongest characteristic emission of Eu^{3+}. This phosphor can be used as a single-component tunable white phosphor in white LEDs.

References

1. D.Q. Chen, W.D. Xiang, X.J. Liang, J.S. Zhong, H. Yu, M.Y. Ding, H.W. Lu, Z.G. Ji, J. Eur. Ceram. Soc. **35**(3), 859–869 (2015)
2. H.C. Cheng, J.Y. Lin, W.H. Chen, Appl. Therm. Eng. **38**(1), 105–116 (2012)
3. C.C. Lin, R.S. Liu, J. Phys. Chem. Lett. **2**(11), 1268 (2011)
4. S. Pimputkar, J.S. Speck, S.P. DenBaars, S. Nakamura, Nat. Photon. **3**(4), 180–182 (2009)
5. X.H. He, J. Zhou, N. Lian, M.Y. Guan, Silicon Bull. **28**(4), 741–750 (2009)
6. D.R. Cooper, J.A. Capobianco, J. Seuntjens, Nanoscale **10**(16), 7821–7831 (2018)

7. J. Cheng, J. Zhang, H.C. Zhang, S. Maryam, X.T. Bian, Z.H. Shen, X.W. Ni, J. Lu, Chin. Opt. Lett. **15**(12), 121602 (2017)

8. L.J. Ren, X.H. L, X.Q. Du, L. Jin, W.M. Chen, Y.A. Feng, J. Lumin. **142**(8), 150–154 (2013)

9. C.F. Zhu, Y.X. Yang, X.L. Liang, S.L. Yuan, G.R. Chen, J. Lumin. **126**(2), 707–710 (2007)

10. D. Ghosh, K. Biswas, S. Balaji, K. Annapurna, J. Alloy. Compd. **747**, 242–249 (2018)

11. T.C. Lang, T. Han, L.L. Peng, M.J. Tu, Mater. Chem. Front. **1**, 928–932 (2017)

12. H.D. Nguyen, C. Lin, M.H. Fang, R.S. Liu, J. Mater. Chem. C **2**(48), 10268–10272 (2014)

13. P.G. Sennikov, S.K. Ignatov, A.E. Sadov, A.G. Razuvaev, O. Schrems, Russ. J. Inorg. Chem. **54**(2), 252–259 (2009)

14. J.J. Cao, B. Li, P.Y. Jia, Funct. Mater. **12**, 12097–12101 (2014)

15. K. Li, H. Lian, M. Shang, J. Lin, Dalton Trans. **44**(47), 20542–20550 (2015)

16. J.L. Zhang, G.Y. Hong, Chin. J. Lumin. **12**(3), 224–229 (1991)

17. D.Z. Xu, J. Feng, X.Y. Yang, E.D. Zu, X.Y. Cui, J.C. Lin, W. Dong, Spectrosc. Spectr. Anal. **37**(06), 1804–1808 (2017)

18. W.Y. Zhang, Q. Jing, Y. Fang, Z.H. Chen, Z. Für. Anorg. Und Allg. Chem. **643**(22), 1739–1743 (2017)

19. D.J. Wei, A.J. Tang, P. Shen, B. Liao, Guizhou Chem. Ind. **36**(05), 32–34 (2011)

20. R. Hoshino, S. Adachi, J. Appl. Phys. **114**, 213502 (2013)

21. J.Q. Ning, C.C. Zheng, L.X. Zheng, S.J. Xu, J. Appl. Phys. **118**, 073101 (2015)

22. J.Q. Ning, S.J. Xu, D.P. Yu, Y.Y. Shan, S.T. Lee, Appl. Phys. Lett. **91**, 103117 (2007)

23. X. Qiao, H.J. Seo, Mater. Res. Bull. **49**(1), 76–82 (2014)

24. P.C. Korir, F.B. Dejene, Appl. Phys. A **124**(5), 356 (2018)

25. C.S. Shi, S.Q. Man, J.Y. Sun, J. Rare Earths **1**, 35–38 (1991)

26. D.K. Singh, J. Manam, Appl. Phys. A **124**(3), 261 (2018)

27. X.F. Wang, C. Zhang, C.Y. Deng, Chin. J. Lumin. **37**(9), 1037–1042 (2016)

28. X.G. Wang, Z.Y. Yu, M. Namira, S.L. Bo, Chin. J. Inorg. Chem. **24**(4), 571–575 (2008)

29. Z.P. Yang, Z. Guo, S.C. Zhu, W.J. Wang, Spectrosc. Spectr. Anal. **24**(12), 1506–1510 (2004)

30. W.N. Zhao, Z.M. Xu, T.Y. Sun, X.H. Wu, S.S. Liu, Z.C. Ma, Solid State Commun. **178**(1), 42–45 (2014)

31. C.H. Zhang, H.B. Liang, S. Zhang, C.M. Liu, D.J. Hou, L. Zhou, G.B. Zhang, J.Y. Shi, J. Phys. Chem. A **116**(30), 15932–15937 (2012)

32. X.G. Wang, Spectrosc. Spectr. Anal. **28**(2), 260–264 (2008)

33. S.L. Ji, L.L. Yin, G.D. Liu, L.D. Zhang, C.H. Ye, J. Phys. Chem. C **113**(37), 16439–16444 (2009)

34. X.Y. Huang, B. Li, H. Guo, J. Alloy. Compd. **695**, 2773–2780 (2017)

35. X.G. Zhang, L.Y. Zhou, Q. Pang, J.X. Shi, M.L. Gong, J. Phys. Chem. C **118**(14), 7591–7598 (2014)

36. K.L. Qiu, H.Z. Lian, Y.Q. Han, M.M. Shang, R.V. Deun, J. Lin, Dyes Pigments **139**, 701–707 (2016)

37. Y.P. Tong, T. Chen, Spectrosc. Spectr. Anal. **33**(11), 2930–2934 (2013)

38. B.L. Wang, L.Z. Sun, H.D. Ju, Solid State Commun. **150**(31), 1460–1462 (2010)

39. F.P. Zhuo, W. Zhang, J.M. Huo, Y.L. Zhao, W. Wu, X. Ding, Y.R. Shi, Y.H. Wang, J. Lumin. **33**(3), 238–242 (2012)

40. B.H. Li, J. Yang, J. Wang, M.M. Wu, Opt. Mater. **36**(10), 1649–1654 (2014)

41. U. Balderas, S. Carmona, L. Mariscal, I. Martínez, C. Falcony, Chem. Phys. **511**, 1–6 (2018)

42. J. Li, Z.Y. Mao, D.J. Wang, Y.C. Zhu, L. Gan, F.F. Xu, Ceram. Int. **39**(8), 9809–9813 (2013)

43. J. Wu, J.L. Zhang, W.L. Zhou, C.Y. Rong, L.P. Yu, C.Z. Li, S.X. Lian, Chem. J. Chin. Univ. **34**(2), 306–312 (2013)

44. S.Y. Kim, K. Woo, K. Lim, K. Lee, H.S. Jang, Nanoscale **5**(19), 9255–9263 (2013)

45. D. Jia, W. Jia, X.J. Wang, W.M. Yen, Solid State Commun. **129**(1), 1–4 (2004)

46. B. Li, X.Y. Huang, Ceram. Int. **44**, 2915–4923 (2017)

47. M. Shang, G. Li, X. Kang, D. Yang, D. Geng, L. Jun, ACS Appl. Mater. Interfaces **3**(7), 2738–2746 (2011)

48. L. Jin, X.Q. Du, X.H. Lei, L.J. Ren, Y.A. Feng, W.M. Chen, Appl. Phys. A **114**(2), 631–636 (2014)

49. S.L. Zhao, F.X. Xin, S.Q. Xu, D. Deng, L.H. Huang, H.P. Wang, Y.J. Hua, J. Non Cryst. Solids **357**(11), 2424–2427 (2011)